Richtmyer–Meshkov instability on a dual-mode interface

Xisheng Luo[1], Lili Liu[1], Yu Liang[1], Juchun Ding[1],† and Chih-yung Wen[2]

[1]Advanced Propulsion Laboratory, Department of Modern Mechanics,
University of Science and Technology of China, Hefei 230026, PR China

[2]Department of Mechanical Engineering and Interdisciplinary Division of Aeronautical and Aviation
Engineering, The Hong Kong Polytechnic University, Kowloon, Hong Kong, PR China

We report the first shock-tube experiments on dual-mode Richtmyer–Meshkov instability (RMI). An extended soap-film technique is adopted to generate a dual-mode gaseous interface such that its initial wavenumber (k_0) and phase of the fundamental waves are well controlled. By extracting interfacial contours from the distinct schlieren images, a Fourier analysis is performed from linear to weakly nonlinear stages and the growth of each basic wave is obtained. A noticeable difference between the growth of each basic mode and the corresponding single-mode RMI is observed, which suggests evident mode coupling effects in the dual-mode RMI. For dual-mode interfaces with in-phase k_0 and $k_0/2$ waves, the mode coupling suppresses (promotes) the growth of the k_0 ($k_0/2$) mode, while for interfaces with anti-phase k_0 and $k_0/2$ modes, the growth of the k_0 ($k_0/2$) mode is weakly influenced (evidently inhibited). However, for the combination of k_0 and $k_0/3$ waves, the mode coupling has a negligible influence on the growth of each basic wave. The modal theory of Haan (*Phys. Fluids* B, vol. 3, 1991, pp. 2349–2355), originally for multi-mode Rayleigh–Taylor instability, is reformulated for the dual-mode RMI, and it is found that this model overestimates the present experimental results for ignoring the nonlinear saturation. This model is then modified by accounting for both the mode coupling and nonlinear saturation, which well predicts the experimental results not only for the growth of the basic waves but also for the growth of second harmonics.

Key words: shock waves

1. Introduction

Richtmyer–Meshkov instability (RMI) (Richtmyer 1960; Meshkov 1969) develops when a corrugated interface between two different fluids is subjected to a shock wave. After the shock impact, perturbations that are inherent on the initial interface grow continuously with time and eventually a flow transition to turbulent mixing is induced. In recent decades, the RMI has become a subject of active research due to its crucial role in natural and engineering situations, e.g. the instability growth is favourable for supersonic combustion (Yang, Kubota & Zukoski 1993) but unfavourable for inertial confinement fusion (ICF) (Lindl *et al.* 2014).

† Email address for correspondence: djc@ustc.edu.cn

A typical but simple RMI is the one on a single-mode interface, which has been extensively studied due to its fundamental significance. Under the assumption of incompressible and inviscid flow, an impulsive model for the early-stage perturbation development was first derived through a linear stability analysis (Richtmyer 1960). Since then, several linear models considering more effects such as compressibility (Wouchuk 2001), three-dimensionality (Luo, Wang & Si 2013) and density ratio (Meyer & Blewett 1972) were proposed to give a better prediction. As the perturbation amplitude grows to a magnitude comparable to the wavelength, nonlinearity becomes pronounced and the symmetry of the interface is broken. To predict the nonlinear growth, numerous high-order models based on the perturbation expansion method (Vandenboomgaerde, Gauthier & Mügler 2002; Zhang, Deng & Guo 2018) and potential models based on the bubble dynamics theory (Sadot *et al.* 1998; Sohn 2003; Zhang & Guo 2016) were developed. Recently, these models have been thoroughly examined by a series of high-fidelity experiments (Liu *et al.* 2018).

However, in real applications, a material interface usually presents multi-mode or random perturbations. In addition to the common flow regimes presented in the single-mode RMI, the multi-mode case includes mode coupling effects such as harmonic generation and bubble merger, and thus possesses much more complex phenomena and mechanisms (Rikanati, Alon & Shvarts 1998; Niederhaus & Jacobs 2003; Sohn 2008; Leinov *et al.* 2009; Di Stefano *et al.* 2015; McFarland *et al.* 2015; Mohaghar *et al.* 2017). In general, the evolution of the multi-mode RMI can be divided into three stages: the linear stage, the mode competition stage and the bubble merger stage. At the linear stage, each basic mode develops independently as that of an isolated mode. At the early nonlinear stage, the basic modes start to interact with each other, and to create new modes with higher or lower wavenumbers, i.e. harmonic generation, and reversely the newly generated modes provide a feedback on the growth of each basic mode. At late nonlinear stages, bubble merger occurs, which corresponds to the process that a large bubble overtakes a small one and finally the two bubbles merge into a larger bubble (Sadot 2017).

Two complementary types of models have been developed to evaluate the growth of the multi-mode RMI: modal models applicable to the early nonlinear stage when the harmonic generation is significant, and statistical-mechanics bubble merger models suitable for the late-time growth. Specifically, modal models consider the interface perturbation as a superposition of various Fourier modes. As has been found by Haan (1991), the neighbouring modes could create a local large structure, which suffers a great kinematic drag and, consequently, the nonlinear saturation occurs at individual mode amplitude much lower than the single-mode counterpart. Later, the validity range of this model was extended by Ofer *et al.* (1996), and the difference between cases with and without mode generation was analysed. Also, based on a simplified perturbation expansion, Vandenboomgaerde *et al.* (2002) derived an analytical solution for the weakly nonlinear growth of multi-mode RMI. As another type, the bubble merger models treat the distorted interface as an ensemble of bubbles arranged along a line, and each bubble rises at an asymptotic velocity proportional to its wavelength as suggested by potential flow theory (Hecht, Alon & Shvarts 1994; Goncharov 2002). Hence, large bubbles expand faster and gradually merge the neighbouring small ones, generating new larger bubbles, i.e. an inverse cascade in wavenumber space. Based on the bubble merger model and given a specified merging rate, a scaling law was derived by Alon *et al.* (1995) for the growth of the mixing zone width at late stages. Nowadays, measuring the constants of the scaling law is still an active research topic (Thornber *et al.* 2017; Reese *et al.* 2018; Thornber *et al.* 2010). Owing to the substantial lack of experimental results, direct validations of these

theories for the multi-mode RMI going from the linear to nonlinear regimes are scarce but very desirable.

The main difficulty for performing an experimental study on the multi-mode RMI, especially in a shock-tube circumstance, lies in creating an idealized initial interface, because the RMI is extremely sensitive to the initial condition of the interface. In the past few decades, numerous techniques and methods have been developed to generate a controllable material interface. Generally, the interfaces formed can be divided into two categories: discontinuous interface (Mariani *et al.* 2008) and diffuse interface (Jacobs & Krivets 2005; Balakumar *et al.* 2012). It has been demonstrated that existing techniques introduce inevitably some imperfections on the initial interface, such as a diffusion layer, undesired perturbations and three-dimensionality, and thus greatly contaminate the development of instability. To overcome these problems, recently, a novel soap-film technique to form sharp interfaces with an idealized single-mode shape has been developed (Liu *et al.* 2018), and the results showed a substantial elimination of these interfacial defects. Further, we performed experiments on quasi-single-mode interfaces formed by the same soap-film technique (Liang *et al.* 2019). It was found that the fundamental mode dominates the initial quasi-single-mode interface and, consequently, the effect of high-order modes on the amplitude growth can be ignored in the linear stage. In the nonlinear stage, high-order modes start to play a role such that all the nonlinear models suitable for single-mode RMI deviate. By considering the effects of high-order modes, the nonlinear model of Zhang & Guo (2016) is modified to predict the growth of the quasi-single-mode interface in the weakly nonlinear stage. It was concluded that more high-order modes are needed to match the experiment as the deviation of the interface shape from the single-mode one is more pronounced. However, for a multi-mode interface without a dominant mode, e.g. an interface with two modes of equivalent amplitude, mode coupling exists from the very beginning of the interface evolution, so that all the linear and nonlinear models need re-examination, which motivates the present work.

In this work, the soap-film technique (Liu *et al.* 2018) will be extended to generate a dual-mode interface with equivalent amplitudes and precisely controlled phases for the fundamental modes such that the dual-mode RMI can be carefully examined. Four dual-mode air/SF$_6$ interfaces with different wave compositions and relative phases between the fundamental waves are realized, and their interactions with a planar shock are captured by high-speed schlieren photography. The perfect initial conditions created as well as the negligible influence of the soap film enable us to obtain high-fidelity experimental results of the dual-mode RMI, which facilitates a reliable extraction of the interfacial contours. The growth of each basic mode is then obtained by a Fourier analysis of the interfacial morphologies. It is expected that a noticeable difference will be observed between the growth of each basic mode and the corresponding single-mode RMI induced by mode coupling effects in a dual-mode RMI. A modal model for the dual-mode RMI will be modified by accounting for both the mode coupling and the nonlinear saturation, and will be validated by comparison with the experimental results.

2. Experimental methods

The experiments are conducted in a horizontal shock tube consisting of a driver section, a driven section, a transformation channel and a test section with a rectangular cross-section (140 mm × 7 mm). This tube has been widely used in shock dynamics and shock-interface interaction studies (Ding *et al.* 2017). As shown in figure 1(*a*), two transparent devices with an inner height of 7.0 mm and a width of 140.0 mm are first made using acrylic plate (3.0 mm thick). A groove (1.0 mm in thickness and 0.5 mm in width)
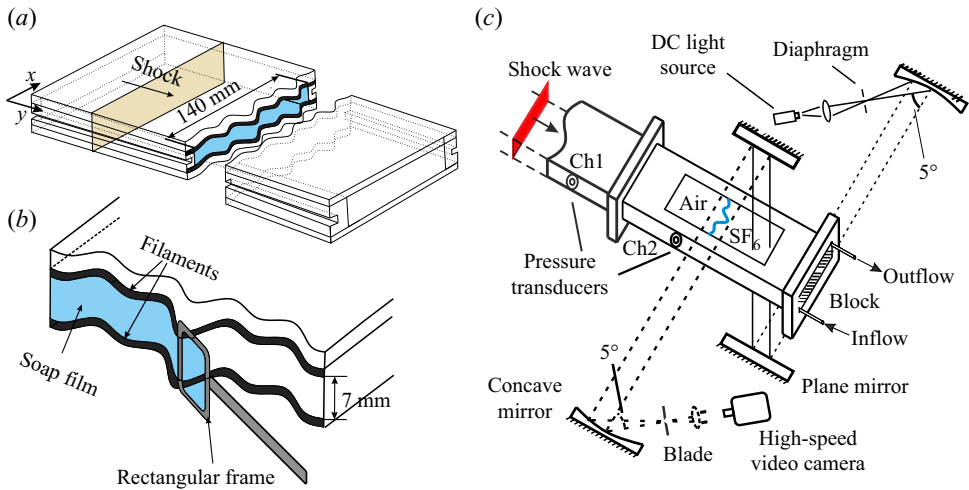
FIGURE 1. Schematics of experimental method and set-up: (*a*) the test section, (*b*) the soap-film technique and (*c*) the schlieren photography adopted in the experiment.
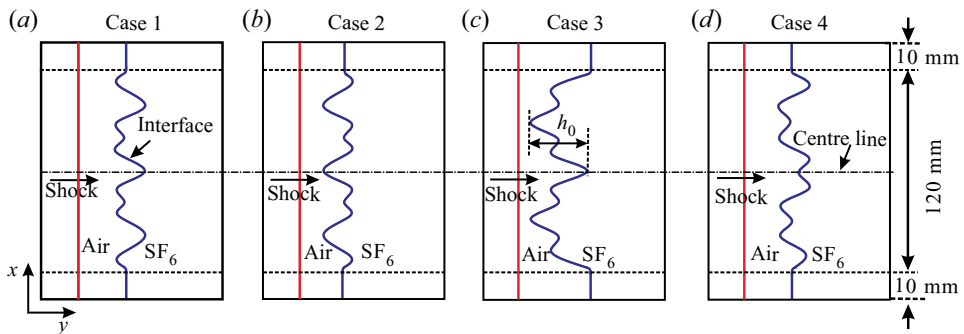

FIGURE 2. Schematics of the four initial interface configurations studied in the present work (not drawn to scale). Here h_0 is the initial total width of the interface.

with a desired dual-mode shape is then manufactured on the internal side of each plate by a high-precision engraving machine. Then two thin filaments (0.75 mm in thickness and 0.5 mm in width) with the same dual-mode profile are mounted into the grooves of the upper and lower plates, respectively, to produce desired constraints. Note that the protrusion height of each filament into the tube is less than 0.3 mm, so that the filaments have a negligible influence on the flow field.

As a small rectangular frame wetted by soap solution (78 % distilled water, 2 % sodium oleate and 20 % glycerine by mass) is pulled along the filaments, a dual-mode soap film is immediately generated (figure 1*b*). Subsequently, the longer device with a soap film on its boundary is inserted gently into the test section and later the shorter one is also inserted until a perfect contact between the two devices is attained. To form an air/SF_6 interface, gaseous SF_6 is injected continuously into the test section through a lower hole and the air is exhausted from an upper hole (figure 1*c*). In this way, a sharp air/SF_6 interface with a desired dual-mode shape is produced. In each experimental run, a gas concentration detector is placed at the exit of the upper hole to measure the volume fraction of O_2 in

Case	λ_1	a_{01}	λ_2	a_{02}	ϕ	h_0	A^+	MF	v_i	Δv	v_f	v_t
1	20.0	1.00	40.0	1.00	0	3.13	0.64	0.95	414.3	76.5	308.4	195.6
2	20.0	1.00	40.0	1.00	π	3.13	0.61	0.92	413.1	77.4	305.3	206.0
3	20.0	1.00	60.0	1.00	0	4.00	0.62	0.93	415.7	78.1	307.2	202.3
4	20.0	1.00	60.0	1.00	π	3.08	0.61	0.92	414.3	79.5	303.3	207.6

TABLE 1. Initial parameters of four dual-mode cases: λ_1 (λ_2) is the wavelength of the first (second) fundamental mode; a_{01} (a_{02}) is the initial amplitude of the first (second) fundamental mode; ϕ is the relative phase between two fundamental modes; h_0 is the initial total width of the interface; A^+ is the post-shock Atwood number; MF denotes the mass fraction of SF_6; v_i is the incident shock velocity; Δv is the interface jump velocity by the shock impact; and v_f and v_t are the velocities of reflected shock and transmitted shock, respectively. The units for length and velocity are mm and m s^{-1}, respectively.

the gas mixture flowing from the upper hole. Once the volume fraction of O_2 is less than 4 %, the gas mixture in the test section is regarded as high-concentration SF_6. To facilitate the interface formation, a short flat part on each side of the perturbed interface is adopted (shown in figure 2) and its effect on the interface evolution is limited (Luo *et al.* 2019).

In a Cartesian coordinate system, a dual-mode interface can be parametrized as $y = a_1 \cos(k_1 x + \phi) + a_2 \cos(k_2 x)$, where a and k denote the initial amplitude and wavenumber of the fundamental mode, respectively, subscripts 1 and 2 refer to the first and second fundamental modes, respectively, and ϕ is the relative phase between the two modes. To illustrate the influences of the initial wavenumber and relative phase, four different dual-mode interfaces are designed in this work and they are expressed as

$$
\left.
\begin{aligned}
\text{case 1:} \quad & y = a_{01} \cos(k_0 x) + a_{02} \cos(k_0 x/2), & x \in [-60, 60] \text{ mm,} \\
\text{case 2:} \quad & y = a_{01} \cos(k_0 x + \pi) + a_{02} \cos(k_0 x/2), & x \in [0, 120] \text{ mm,} \\
\text{case 3:} \quad & y = a_{01} \cos(k_0 x) + a_{02} \cos(k_0 x/3), & x \in [-60, 60] \text{ mm,} \\
\text{case 4:} \quad & y = a_{01} \cos(k_0 x + \pi) + a_{02} \cos(k_0 x/3), & x \in [0, 120] \text{ mm,}
\end{aligned}
\right\}
\tag{2.1}
$$

where $k_0 = 2\pi/20 \text{ mm}^{-1} = 314.16 \text{ m}^{-1}$ is adopted for the present experiments.

The experimental configurations for the four dual-mode interfaces impacted by a planar shock are schematically shown in figure 2 (not drawn to scale). To obtain a symmetric evolution of the interface, the initial dual-mode interface is set to be symmetric along the centreline of the test section, which explains the variation of the x range in equations (2.1) for different dual-mode interfaces. Detailed parameters corresponding to the initial conditions for each case are listed in table 1: λ_1 and λ_2 are the wavelengths of two fundamental modes, respectively; a_{01} and a_{02} are the corresponding initial amplitudes; h_0 is the initial total width of the interface; $A^+ = (\rho_2^+ - \rho_1^+)/(\rho_2^+ + \rho_1^+)$ is the post-shock Atwood number, with ρ_2^+ and ρ_1^+ being the post-shock densities of SF_6 and air on the right and left sides of the interface, respectively; and MF denotes the mass fraction of SF_6 on the right side of the interface. Note that the mass fraction of SF_6 is estimated according to one-dimensional gas dynamics theory, with the measured speeds of the incident shock propagating in pure air on the left side of the interface and the transmitted shock moving in the gas mixture on the right side.

The main reasons for the gas pollution are given below. First, the air on the right side of the interface cannot be completely exhausted from the test section, as indicated by

the volume fraction of O_2 (monitored by the gas concentration detector), which is always higher than 2 %. Second, air molecules on the left side of the interface could pass across the soap film and then contaminate the SF_6 on the other side. Despite the gas pollution, a high concentration of SF_6 is achieved in each experimental run and the difference in SF_6 mass fraction among cases 1–4 is within 3.4 %. The initial amplitude-to-wavelength ratio (a_{01}/λ_1 and a_{02}/λ_2) for each basic wave is less than 0.1, which satisfies the small perturbation assumption (Chapman & Jacobs 2006). Since nonlinear behaviour (i.e. mode coupling) of the RMI is mainly related to the amplitude-over-wavelength ratio rather than to dimensional quantities such as amplitude and wavelength, only one value for k_0 (a_0) is adopted in the present experiments. If we adopt other values for k_0 (a_0) but maintain the same initial amplitude-over-wavelength ratio for each basic mode, the normalized results would remain the same. The incident shock Mach number measured by two piezoelectric transducers is 1.21 ± 0.01. The flow field is monitored by high-speed schlieren photography. The frame rate of the high-speed video camera (FASTCAM SA5, Photron Ltd) is set as 50 000 frames per second, with a shutter time of 1 µs. The spatial resolution of the schlieren images is 0.28 mm pixel^{-1}. The ambient pressure and temperature are 101.3 ± 0.1 kPa and 295.0 ± 2.0 K, respectively.

Since in the present experiments the incident shock is weak, the post-shock flow can be assumed to be laminar and incompressible. Thus, the thickness of the boundary layer at the wall of the shock tube in the post-shock flow (δ^*) can be estimated by

$$\delta^* = 1.72\sqrt{\frac{\mu x}{\rho \Delta v}}. \tag{2.2}$$

Here, $x = 100$ mm is adopted, which corresponds to the maximum distance travelled by the interface during the experimental time. The viscosity coefficient and density of pure air (SF_6) under the experimental temperature and pressure are $\mu = 1.83 \times 10^{-5}$ Pa s (1.60×10^{-5} Pa s) and $\rho = 1.204$ kg m^{-3} (6.143 kg m^{-3}), respectively. The velocity of the post-shock flow is $\Delta v = 80.0$ m s^{-1} calculated by one-dimensional gas dynamics theory. According to (2.2), the maximum thickness of the boundary layer is calculated to be approximately 0.22 mm in the air flow (0.09 mm in the SF_6 flow), which is much smaller than the inner height of the test section (7.0 mm). It indicates a negligible influence of the boundary layer on the interface development. This is confirmed by experimental observation (figure 3) that the interfacial morphologies at late stages when the boundary layer has become relatively thicker are as clear and distinct as those at early stages when the boundary layer just starts developing.

Note that compressibility effect on the post-shock flow should be considered when the incident shock has a Mach number higher than 1.4. The laminar post-shock flow in the present experiment is supported by the following analysis. Generally, there are two types of flows: steady-state flow and time-dependent flow. According to Dimotakis (2000), for steady-state flows, mixing transition (i.e. rapid mixing at atomic scale) occurs when the Reynolds number exceeds a critical value (1–2×10^4). For time-dependent flows such as the RMI problem, Zhou *et al.* (2003, 2019) found that two conditions must be met to achieve the mixing transition: (i) the flow Reynolds number is greater than a critical value, and (ii) sufficient evolution time is needed to allow the formation of an inertial range whose upper bound of wavenumber is significantly larger than the lower bound. In this work, we only focus on the instability development from early to weakly nonlinear stages when the flow is still laminar.
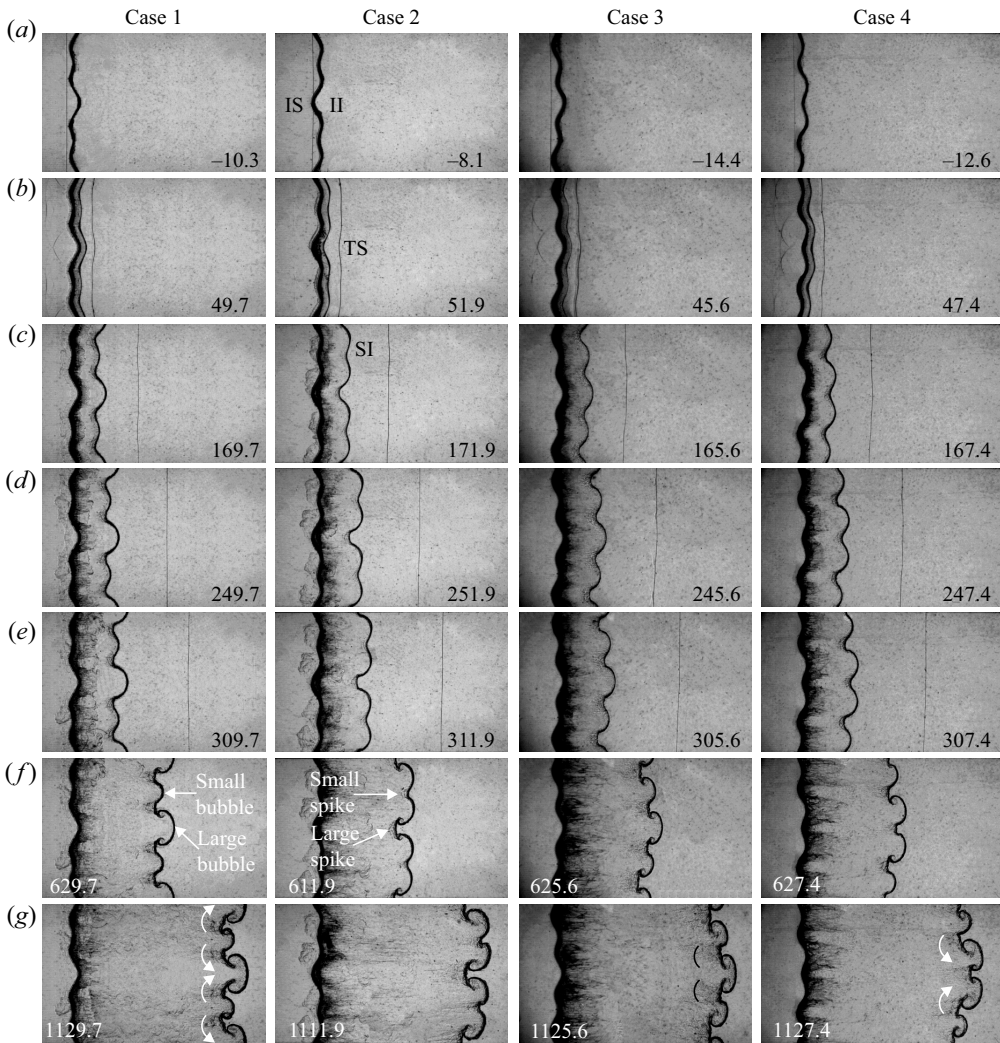
FIGURE 3. Schlieren pictures illustrating the dual-mode interface evolution for cases 1–4. Numbers denote the time in μs, and $t = 0$ is defined as the moment when the incident shock arrives at the mean position of the initial interface. IS, incident shock; II, initial interface; SI, shocked interface; TS, transmitted shock. Arrows in the last row indicate the tilt of the spike during the evolution.

3. Results and discussion

3.1. *Interface morphology*

The dynamic evolution of the interface and the waves for all cases is clearly captured by the high-speed video camera. As shown in figure 3, the interfacial morphologies obtained are much more distinct than those of previous experiments (Sadot *et al.* 1998; Mariani *et al.* 2008), which greatly facilitates the measurement of perturbation amplitudes and the extraction of interface contours.

Here, we take case 2 (the anti-phase interface, $\phi = \pi$) as an example to detail the evolution process. This anti-phase interface has a large spike at the centre and a small one located on each side. The time origin in this work is defined as the moment when

the incident shock arrives at the mean position of the initial interface. At the beginning (-8.1 µs), the initial interface (II) looks rather thick because in the schlieren image the interface is covered by the two dual-mode filaments (0.5 mm in width), which are mounted, respectively, on the upper and lower observation windows. When the incident shock (IS) passes across the interface, the incident shock bifurcates into a downstream-propagating transmitted shock (TS, which is slightly deformed due to the imprint by the dual-mode interface) and an upstream-moving reflected shock (RS, which soon exits the visualization window). Subsequently, the shocked interface (SI) leaves its original location, and a clean density interface with a perfect dual-mode shape can be observed (171.9 µs). We note that both the transmitted shock and the shocked interface look rather thin and clear as expected. This demonstrates the good feasibility and reliability of the current experimental methods. As time proceeds, the transmitted shock recovers to a planar shape while the shocked interface undergoes sustained deformation due to the deposition of baroclinic vorticity, causing a continuous increment in perturbation amplitude. At late stages, a finger-like spike and bubble structures arise due to the increasing nonlinearity, and later each spike rolls up with a pair of vortices formed at its neck (611.9 µs). In this anti-phase case, all the bubbles initially possess the same shape and size, and then develop symmetrically during the experimental time. Also, the spikes with two different initial sizes present a symmetric evolution. After 611.9 µs, the large spike rolls up evidently similar to that of the single-mode RMI, while the development of the small spike is largely suppressed and no roll-up structures appear.

Different from the anti-phase case (case 2), the in-phase interface (case 1) initially has a large bubble at the centre and a small one located on each side. It is observed that after the shock impact, the large bubble experiences a much faster growth than the small ones, i.e. the absolute growth rate of the larger bubble is higher than that of the smaller one. This provides strong evidence for the prediction from the potential flow theory (Goncharov 2002), i.e. the growth rate of a bubble at late stages is proportional to its lateral dimension. As time proceeds, the large bubble gradually invades the adjacent small ones and, consequently, the spikes develop with an apparent inclination to the large bubble. Such an inclination emerges at 309.7 µs and becomes noticeable at 629.7 µs. Also, the roll-up of the spikes is evident on the large bubble side, while the one on the small bubble side is too small to be discerned. These results indicate that the initial size and distribution of bubbles at a dual-mode interface (closely related to the phase difference between two basic modes) significantly affect the bubble growth and further the spike evolution.

As shown in cases 3 and 4, for the k_0–$k_0/3$ wave compositions, some of the spikes develop symmetrically while the others develop asymmetrically. Hence, the evolving interfacial morphologies for these cases are far more distorted than the k_0–$k_0/2$ situation. This suggests a crucial influence of the basic wave compositions on the development of dual-mode RMI. Also, a noticeable discrepancy between cases 3 and 4 for the interface structure evolution is observed, which reveals again a strong influence of the phase difference between two basic modes on the dual-mode RMI. As indicated by the arrows in the last row of figure 3, the spikes are inclined to the large bubble, and roll up only on the large bubble side, which is similar to that in case 1.

Since in the current experiments the shape of the initial interface can be precisely controlled and also the gas concentration on each side of the interface varies slightly from run to run, the experimental results have a good repeatability, especially for the evolution of intermediate- and larger-scale structures. Note that small-scale structures are not observable in the present experiments due to the limitation of the schlieren imaging technique and the limited spatial resolution of the high-speed camera. In this work, we only focus on the growth of intermediate- and large-scale structures from linear to

weakly nonlinear stages, and thus the corresponding analysis is reliable. A detailed study on the developments of small-scale structures requires the application of more advanced imaging techniques, such as planar laser-induced fluorescence, which is ongoing in our group.

3.2. *Growth of perturbation amplitude and mixing width*

Clear interfacial morphologies obtained in the schlieren images demonstrate that the initial interfacial imperfections in previous experiments such as short-wavelength perturbations, diffusion layer and three-dimensionality are largely eliminated by the novel soap-film technique in this study. Therefore, the present experimental results are of high fidelity and, we believe, they are of great use for validating the existing theories and algorithms and also for analysing the mode coupling effect (Ofer *et al.* 1996; Vandenboomgaerde *et al.* 2002).

Clear interface contours can be extracted from the schlieren images by a digital image processing procedure including four steps. First, the original schlieren images in RGB colour pattern are converted to those in greyscale pattern. Next, the initial schlieren image prior to the shock arrival is subtracted from the shocked images such that the background noise (e.g. the dual-mode filaments) can be removed. Afterwards, the profiles of the shocked interfaces are recovered through efficient matrix operations and appropriate image intensification. Finally, the coordinates of these interface contours are extracted by identifying regions of the largest greyscale gradient. After this, the amplitude growth of each basic wave can be obtained by performing a serial Fourier analysis of the extracted interfacial contours (insets in figure 6). Because the Fourier decomposition is applicable only to single-valued functions, here only the temporal variation of amplitude prior to the emergence of roll-up ($t < 370$ µs, corresponding to the early nonlinear stage) can be obtained.

The variations of the dimensionless perturbation amplitudes of the basic modes versus dimensionless time are shown in figure 4. The amplitude is normalized as $\alpha = (a - a^*)/a_0$, and the time is scaled as $\tau = v^{lin}(t - t^*)/a_0$, where $v^{lin} = k\Delta v A^+ a_0^+$ is the linear growth rate calculated by the impulsive model (Richtmyer 1960). Here, t^* stands for the characteristic time of the startup phase according to Lombardini & Pullin (2009), a^* is the corresponding amplitude at t^* and a_0^+ is the interface amplitude just after the shock impact. In this work, the post-shock amplitude, a_0^+, cannot be measured directly from experiment due to the limited temporal resolution of the high-speed camera and thus is estimated by $a_0^+ = a_0(1 - \Delta v/v_i)$. The error bars in figure 4 represent one pixel size of the schlieren images, which blurs the interface profile. For comparison, the amplitude variations with time for the corresponding single-mode RMI predicted by theoretical models are shown in figure 4. The theoretical models adopted are the impulsive model (Richtmyer 1960) and the nonlinear model of Zhang & Guo (2016) (ZG model), and both have been examined by elaborate experimental results (Liu *et al.* 2018) from linear to nonlinear stages.

Overall, it can be seen in figure 4(*a*) that, for case 1, the experimental result of the k_0 wave is lower than the prediction of the ZG model for the corresponding single-mode RMI, while the amplitude of the $k_0/2$ wave is higher than the model prediction. This discrepancy between the experimental result and the model prediction indicates that the mode coupling suppresses the development of the k_0 wave but promotes the growth of the $k_0/2$ wave. However, for case 2 with a relative phase of π between the two basic modes, the mode coupling has a negligible influence on the development of the k_0 mode, but evidently inhibits the growth of the $k_0/2$ mode. The significant difference between
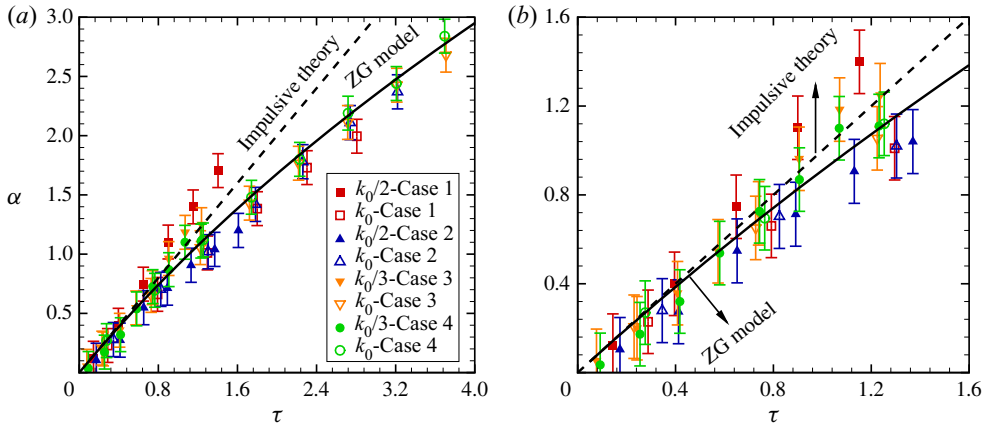
FIGURE 4. Comparison of the dimensionless amplitudes of the two fundamental modes in the four dual-mode cases from linear to nonlinear stages (*a*) and only for the linear stage (*b*). The impulsive model (Richtmyer 1960) and the ZG model (Zhang & Guo 2016) are represented by dashed and solid lines, respectively.

cases 1 and 2 indicates that the relative phase between the two fundamental modes greatly influences the mode coupling, and further affects the growth of each basic mode. This result is in qualitative agreement with the previous findings (Miles *et al.* 2004; Pandian, Stellingwerf & Abarzhi 2017). Differently, for dual-mode interfaces composed of k_0 and $k_0/3$ waves (cases 3 and 4), each basic wave shows nearly the same growth as that of the corresponding single-mode RMI. This indicates a negligible mode coupling effect for the k_0–$k_0/3$ cases. The present finding suggests that for dual- or multi-mode RMI, the effect of mode coupling on the growth of each basic mode at the early nonlinear stage depends heavily on the initial wave compositions.

It is also interesting to compare their behaviours in the linear stage, as shown in figure 4(*b*). Although the error bars in figure 4(*b*) are quite noticeable due to the limited spatial resolution of the high-speed camera, the experimental data before $\tau = 0.7$ for the four dual-mode cases collapse quite well. A linear fitting of the experimental data for the four cases before $\tau = 0.7$ shows a dimensionless growth rate of 0.94 ± 0.04, which agrees reasonably with the prediction of impulsive theory (1.0). This indicates a very weak mode coupling effect at the linear stage of the present dual-mode RMI.

Temporal variations of the overall mixing width (defined in figure 2) of the dual-mode interface for the four cases are given in figure 5. As suggested by Thornber *et al.* (2017), the mixing width here is normalized as $(h - h^*)/\bar{\lambda}$ and the time is scaled as $v_h^{lin}(t - t^*)/\bar{\lambda}$, with h^* being the corresponding mixing width at the time t^*. In the above, $v_h^{lin} = k\Delta v A^+ h_0^+$ is the linear growth rate of mixing width, with h_0^+ being the interface width just after the shock passage and calculated by $h_0^+ = h_0(1 - \Delta v/v_i)$. Finally, $\bar{\lambda}$ denotes the weighted average wavelength, and for its definition the reader is referred to the work of Thornber *et al.* (2017). It is seen in figure 5 that normalized data for the four cases collapse quite well. This suggests a negligible influence of the phases and the wave compositions of a dual-mode interface on the growth of mixing width at early and weakly nonlinear stages.

3.3. *Modal model for dual-mode RMI*

For the evolution of a multi-mode interface, a modal model with second-order accuracy has been proposed to quantify the mode competition effect (Haan 1991). This modal model
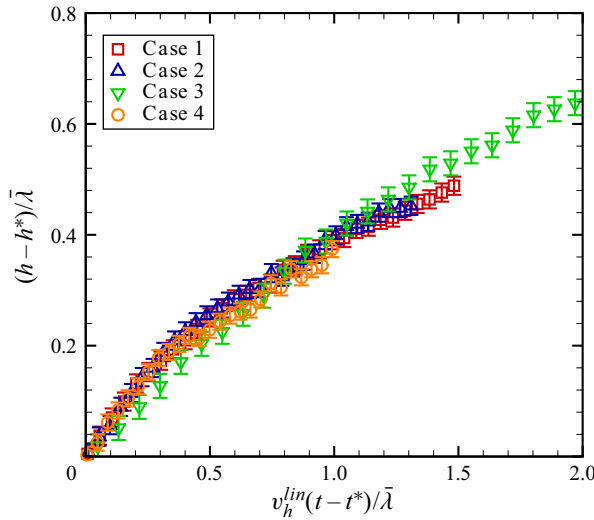
FIGURE 5. Normalized variations of the mixing width of the interface with dimensionless time for the four dual-mode cases. Here h^* is the corresponding mixing width at the time t^* and $v_h^{lin} = k\Delta v A^+ h_0^+$ is the linear growth rate of mixing width, with h_0^+ being the interface width just after the shock passage; and $\bar{\lambda}$ denotes the weighted average wavelength according to Thornber *et al.* (2017).

and its extended type (Ofer *et al.* 1996) have achieved a wide range of validation in the multi-mode Rayleigh–Taylor (RT) instability (Rollin & Andrews 2013; Martinez *et al.* 2015), but its application in RMI is still scarce. In this work, through analysing the growth of each individual mode from linear to weakly nonlinear stages in our experiment, we expect to construct a modal model for the dual-mode RMI.

Under the assumption of incompressible, inviscid and irrotational flow, Haan (1991) derived a second-order modal model for the multi-mode RT instability, which can be written as

$$a_k(t) = a_k^{lin}(t) + \frac{1}{2}kA\left(\sum_{k'}a_{k'}^{lin}(t)a_{k+k'}^{lin}(t) - \frac{1}{2}\sum_{k'<k}a_{k'}^{lin}(t)a_{k-k'}^{lin}(t)\right). \qquad (3.1)$$

Here, $a_k^{lin}(t)$ is the time-dependent amplitude of mode k at the linear stage and can be calculated by the impulsive theory (Richtmyer 1960). The second term on the right-hand side of (3.1) represents the generation of mode k from both shorter-wavelength $(k + k')$ and longer-wavelength $(k - k')$ modes. Note that the modal model is applicable only to the instability growth from linear to weakly nonlinear stages.

Applying this model to a dual-mode RT instability with basic k and $k/2$ modes, the growth of the basic modes and the generated second harmonics can be written as

$$\left.\begin{aligned}
a_{k/2}(t) &= a_{k/2}^{lin}(t) + \tfrac{1}{4}kAa_{k/2}^{lin}(t)a_k^{lin}(t), \\
a_k(t) &= a_k^{lin}(t) - \tfrac{1}{4}kAa_{k/2}^{lin}(t)a_{k/2}^{lin}(t), \\
a_{3k/2}(t) &= -\tfrac{3}{8}kAa_{k/2}^{lin}(t)a_k^{lin}(t), \\
a_{2k}(t) &= -\tfrac{1}{2}kAa_k^{lin}(t)a_k^{lin}(t).
\end{aligned}\right\} \qquad (3.2)$$

Taking the second derivatives of equations (3.2) with time, we get

$$
\left.\begin{aligned}
\frac{\mathrm{d}^2 a_{k/2}(t)}{\mathrm{d}t^2} &= \frac{1}{2}a_{0k/2}gkA + \frac{1}{4}kA\left[a_{k/2}^{lin}(t)a_{0k}gkA + \frac{1}{2}a_k^{lin}(t)a_{0k/2}gkA + \sqrt{2}a_{0k}a_{0k/2}gkA\right], \\
\frac{\mathrm{d}^2 a_k(t)}{\mathrm{d}t^2} &= a_{0k}gkA - \frac{1}{2}kA\left(\frac{1}{2}a_{k/2}^{lin}(t)gkA + \frac{1}{2}a_{0k/2}^2 gkA\right), \\
\frac{\mathrm{d}^2 a_{3k/2}(t)}{\mathrm{d}t^2} &= -\frac{3}{8}kA\left(a_{k/2}^{lin}(t)a_{0k}gkA + \sqrt{2}a_{0k/2}a_{0k}gkA + \frac{1}{2}a_k^{lin}(t)a_{0k/2}gkA\right), \\
\frac{\mathrm{d}^2 a_{2k}(t)}{\mathrm{d}t^2} &= -kA(a_k^{lin}(t)a_{0k}gkA + a_{0k}^2 gkA).
\end{aligned}\right\}
\tag{3.3}
$$

Replacing the constant acceleration g in equations (3.3) with an impulsive acceleration $\delta t \Delta v$ (the shock-induced acceleration) and then integrating (3.3) with time, a modal model for the dual-mode RMI is obtained and expressed as

$$
\left.\begin{aligned}
v_{k/2} &= v_{k/2}^{lin} + \tfrac{1}{2}kA^+(\sqrt{2}v_{k/2}^{lin}a_k^+ + \tfrac{3}{2}v_{k/2}^{lin}v_k^{lin}t), \\
v_k &= v_k^{lin} - \tfrac{1}{2}kA^+(v_{k/2}^{lin}a_{k/2}^+ + v_{k/2}^{lin}v_{k/2}^{lin}t), \\
v_{3k/2} &= -\tfrac{3}{8}kA^+[2v_{k/2}^{lin}v_k^{lin}t + v_{k/2}^{lin}a_k^+ + (1+\sqrt{2})v_k^{lin}a_{k/2}^+], \\
v_{2k} &= -kA^+(v_k^{lin}v_k^{lin}t + 2v_k^{lin}a_k^+).
\end{aligned}\right\}
\tag{3.4}
$$

Figure 6 shows a comparison between the predictions of equations (3.4) and the present experimental results for the growth of each basic wave in cases 1 and 2. It is seen that the modal model for the dual-mode RMI can roughly assess the amplitude variation tendency of each basic mode in experiments. Specifically, for case 1, the mode coupling suppresses the growth of the k_0 wave but promotes the $k_0/2$ wave, and for case 2, the mode coupling has a negligible influence on the growth of the k_0 wave but evidently inhibits the $k_0/2$ wave. These observations can be well explained by the modal model. As indicated in (3.4), for case 1 with basic k_0 and $k_0/2$ modes of positive amplitudes, the self-coupling of the $k_0/2$ wave (the second term on the right-hand side of the second line of (3.4)) generates a new k_0 wave of negative amplitude, and thus suppresses the growth of the basic k_0 mode. Also, the coupling between the k_0 and $k_0/2$ modes produces a new $k_0/2$ mode of positive amplitude (the first line of (3.4)), and thus promotes the development of the basic $k_0/2$ mode. For case 2, where the basic k_0 and $k_0/2$ waves possess negative and positive amplitudes, respectively, the mode coupling produces a new negative k_0 mode (a new positive $k/2$ mode) as indicated in (3.4), and thus promotes (inhibits) the growth of the basic k_0 ($k_0/2$) wave. For a clear presentation, the amplitude signs of the new generated waves predicted by (3.4) and their influences on the growth of basic waves for cases 1 and 2 are listed in table 2.

Although equations (3.4) can qualitatively forecast the mode coupling effects in the dual-mode RMI (i.e. inhibiting or promoting the basic wave growth), they evidently overestimate the amplitude growth of each basic wave for cases 1 and 2. The primary reason is that the analytical solution of Haan (1991) employs a linear growth rate for each basic wave, namely, it ignores the nonlinear saturation on the instability growth. It has been widely recognized that, during the evolution of RMI, nonlinearity becomes increasingly
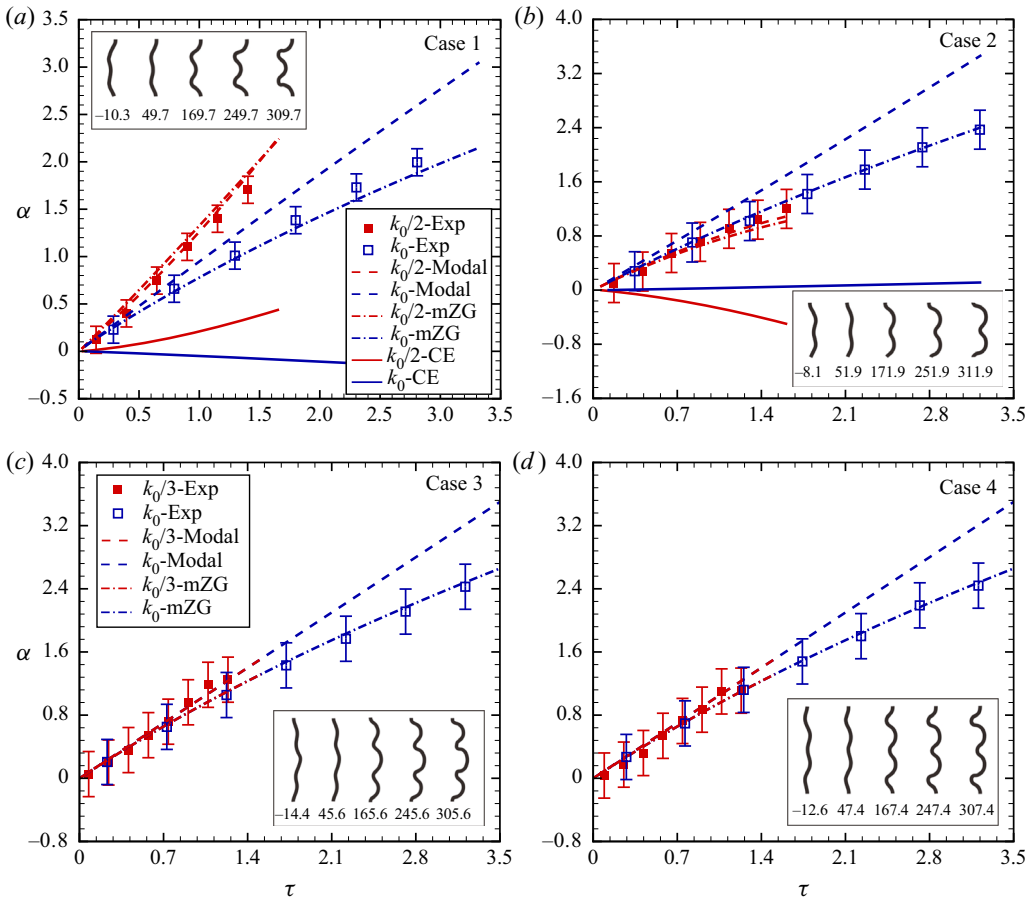
FIGURE 6. Comparison of experimental results with the predictions of modal model (3.4) and the modified Zhang–Guo (mZG) model for the four cases. 'CE' denotes the mode coupling effect. Insets are the interface contours extracted from schlieren images with numbers in μs.

Cases	Basic mode k_0	Basic mode $k_0/2$	Generated k_0	Generated $k_0/2$	k_0 growth	$k_0/2$ growth
1	+	+	−	+	↓	↑
2	−	+	−	−	↑	↓

TABLE 2. The amplitude signs of the new waves generated by mode coupling predicted by equations (3.4) for cases 1 and 2. The $+$ $(-)$ indicates a positive (negative) amplitude and the ↓ (↑) denotes the suppression (promotion) of the growth of the basic wave.

stronger and produces a continuous reduction in perturbation growth rate. Recently, a potential flow model for the nonlinear growth of the bubble and spike of the single-mode RMI has been developed by Zhang & Guo (2016) (ZG model), which is expressed as

$$v(t) = \frac{v_0}{1 + \hat{a}kv_0t}, \tag{3.5}$$

where

$$\hat{a} = \frac{3}{4} \frac{(1+A^+)(3+A^+)}{[3+A^+ + \sqrt{2}(1+A^+)^{1/2}]} \frac{[4(3+A^+) + \sqrt{2}(9+A^+)(1+A^+)^{1/2}]}{[(3+A^+)^2 + 2\sqrt{2}(3-A^+)(1+A^+)^{1/2}]}. \tag{3.6}$$

Here, v_0 is the linear growth rate and $v(t)$ is the time-dependent perturbation growth rate considering nonlinear saturation. The ZG model has been thoroughly validated by both experimental and numerical results (Bai, Deng & Jiang 2018; Liu *et al.* 2018; Zhang *et al.* 2018; Liang *et al.* 2019).

We recognize that a modal model capable of accurately estimating the growth of the basic waves in the dual-mode RMI should take into account both the mode coupling effect and the growth rate reduction caused by nonlinearity. With this guideline, a new modal model for the dual-mode RMI can be constructed. The growth rates of the basic waves and the second harmonics for the dual-mode RMI considering mode coupling have been given in (3.4). Here, to account for the nonlinear saturation, we adopt a treatment similar to that of Zhang & Guo (2016), namely, substitute these growth rates into (3.5) to replace the original v_0 while keeping the other variables and parameters unchanged. In this way, a modified ZG model (mZG) including both mode coupling and nonlinear saturation is obtained. The expression of the mZG model is quite long and not shown here (see appendix A).

Figure 6 shows a comparison of the predictions of the mZG model with the experiments for the growth of the basic modes. As we can see, the new modal model gives a much better prediction of the growth of each basic wave for all cases. Also, we can quantify the effect of mode coupling on the growth of each basic wave by comparing the prediction of the mZG model for dual-mode RMI with the prediction of the ZG model for single-mode RMI. As clearly shown by the solid lines (denoted by 'CE') in figure 6, the mode coupling promotes the growth of the $k_0/2$ wave in case 1, inhibits the k_0 wave in case 1 and the $k_0/2$ wave in case 2, and has a negligible effect on the k_0 wave in case 2. For cases 3 and 4, the corresponding modal model expressions for the growth of the k_0 and $k_0/3$ waves are proved to be equivalent to the single-mode counterparts. As suggested by (3.2) with a second-order accuracy, the k and $k/3$ modes generate $2k/3$ and $4k/3$ modes, and thus produce negligible influences on the growth of each basic wave. As a result, the experimental growth of the k_0 and $k_0/3$ modes are very close to the single-mode result as shown in figure 4, and the prediction of the mZG model coincides with the ZG model for cases 3 and 4 as illustrated in figure 6.

Finally, we examine the developments of the second harmonics in the dual-mode RMI. The corresponding expressions of the mZG model for the growth of the second harmonics for dual-mode interfaces with the basic k_0 and $k_0/3$ modes can be derived simply by following the procedure from (3.2) to (3.6) and, therefore, they are not given here for the sake of brevity. Figure 7 shows a comparison between the experimental results and the predictions of the mZG model for the growth of the second harmonics. Note that the results here are normalized using wavelength as the reference length scale rather than amplitude, because the initial amplitude of each harmonic is zero. At the early stage, the growth of the second harmonics is rather slow, which indicates a weak nonlinearity. Later, as nonlinearity becomes strong, the mode coupling acts evidently and causes an increasingly faster growth of the second harmonics. It is seen that the mZG model reasonably predicts the generation and growth of the second harmonics from early to weakly nonlinear stages for all cases, which further demonstrates its validity in the dual-mode RMI. Although the mZG model can reasonably predict the growth of the second harmonics, there exists
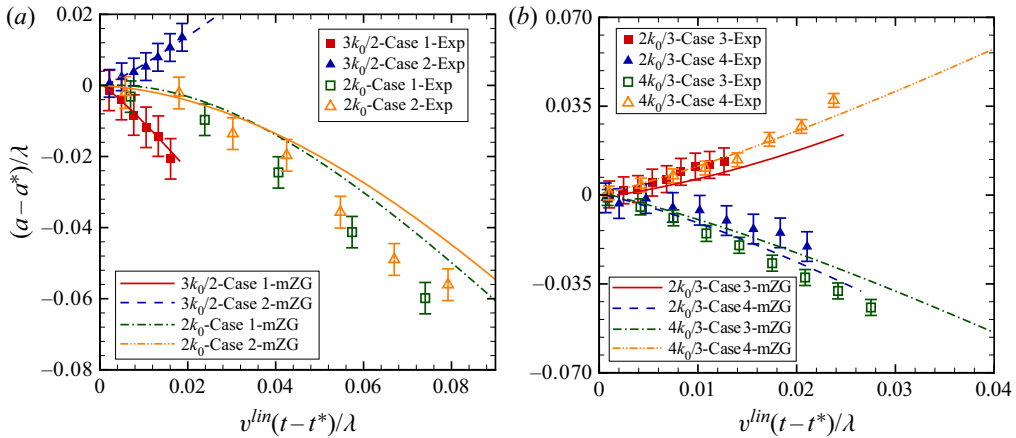
FIGURE 7. Comparison of experimental results with the predictions of the mZG model for the growth of the second harmonics for (*a*) cases 1 and 2 and (*b*) cases 3 and 4.

an evident deviation between the experimental results and model predictions, especially at late stages. Two reasons are responsible for this. First, the original model of Haan (1991), based on which the mZG model is constructed, has only second-order accuracy, which indicates the ignorance of feedback of higher harmonics to the growth of second harmonics. Second, the present mZG model is developed by empirically combining the Haan (1991) model (considering mode coupling) and the ZG model (considering nonlinear saturation), which lacks accurate theoretical modelling and derivation.

The modal model for dual-mode RMI developed in this work can be incorporated into the existing multi-mode models to increase their prediction accuracy. Take the just-saturated model of Groom & Thornber (2020) as an example. The original just-saturated mode (Dimonte, Frerking & Schneider 1995) assumes that each mode on a multi-mode interface grows independently at an impulsive growth rate (Richtmyer 1960) in the early stage and eventually saturates. Thus, short-wavelength modes grow quickly at the early stage and then are overtaken by longer-wavelength modes. As a result, the whole instability growth is dominated by the just-saturated mode growing at its impulsive growth rate. The present study shows that mode coupling is evident at the early stage and should be taken into account. Extending the present dual-mode model to multi-mode situations and then incorporating the growth rate of each basic mode considering mode coupling into the just-saturated mode, a more accurate multi-mode RMI model can be obtained.

4. Conclusions

In this work, the dual-mode RMI is examined in shock-tube experiments for the first time, emphasizing the mode coupling effects on the growth of the basic modes and the second harmonics from linear to nonlinear stages. Four well-controlled dual-mode interfaces with different mode compositions and phases of the basic modes are created by an extended soap-film technique, and clear interfacial morphologies and wave patterns during their evolutions after the impact of a planar shock are well captured by high-speed schlieren photography. The experimental results clearly exhibit the mode competition and bubble merger processes in the dual-mode RMI. It is observed that the spike or bubble develops with an inclination to a certain direction depending on the initial shape of the

dual-mode interface. The size and distribution of the bubbles on the initial dual-mode interface greatly influence the bubble evolution and further the spike growth.

The amplitude growth of the basic modes and the second harmonics are obtained by a serial Fourier analysis of the interfacial contours extracted from the high-quality schlieren images. A noticeable difference between the growth of each basic mode and the corresponding single-mode RMI is observed, which suggests evident mode coupling effects in the dual-mode RMI. The relative phase between the two fundamental modes greatly influences the mode coupling. For dual-mode interfaces consisting of in-phase k_0 and $k_0/2$ modes, the mode coupling suppresses the growth of the k_0 mode but promotes the growth of the $k_0/2$ wave. For interfaces with anti-phase k_0 and $k_0/2$ modes, the mode coupling inhibits the growth of the $k_0/2$ wave but produces only a slight influence on the k_0 wave. However, for the k_0 and $k_0/3$ wave combination, the mode coupling has a negligible influence on the growth of all basic waves regardless of their relative phase.

The modal theory of Ofer *et al.* (1996), originally proposed for the multi-mode RT instability, is reformulated for the dual-mode RMI. It is found that the modal model is capable of roughly assessing the mode competition effect, but it overestimates the amplitude growth of all the basic waves by ignoring the growth rate reduction caused by nonlinearity. A modified modal model accounting for both the mode coupling effect and the nonlinear saturation is then constructed, which gives a much better prediction of the present experimental results not only for the growth of the basic waves but also for the growth of the second harmonics. The mode coupling in the dual-mode RMI with two basic waves of equivalent amplitudes acts earlier and more evidently than that of the multi-mode RMI with an initial dominant mode (Liang *et al.* 2019). The mode coupling process revealed in the dual-mode RMI would be of great use for understanding and modelling the multi-mode RMI. Our work is the first experimental study on the dual-mode RMI in a shock tube, and we believe it is an important step towards the elaborate study on the multi-mode RMI.

Declaration of interests

The authors report no conflict of interest.

Appendix A

The mZG model for the growth of each basic model is expressed as

$$v_{k/2}(t) = \frac{v_{k/2}^{lin} + \frac{1}{2}kA^+\left(\sqrt{2}v_{k/2}^{lin}a_k^+ + \frac{3}{2}v_{k/2}^{lin}v_k^{lin}t\right)}{1 + \hat{a}k\left(v_{k/2}^{lin} + \frac{1}{2}kA^+\left(\sqrt{2}v_{k/2}^{lin}a_k^+ + \frac{3}{2}v_{k/2}^{lin}v_k^{lin}t\right)\right)t}, \tag{A 1}$$

$$v_k(t) = \frac{v_k^{lin} - \frac{1}{2}kA^+ \left(v_{k/2}^{lin}a_{k/2}^+ + v_{k/2}^{lin}v_{k/2}^{lin}t\right)}{1 + \hat{a}k\left(v_k^{lin} - \frac{1}{2}kA^+\left(v_{k/2}^{lin}a_{k/2}^+ + v_{k/2}^{lin}v_{k/2}^{lin}t\right)\right)t}, \tag{A 2}$$

$$v_{3/2k}(t) = \frac{-\frac{3}{8}kA^+\left[2v_{k/2}^{lin}v_k^{lin}t + v_{k/2}^{lin}a_k^+ + (1+\sqrt{2})v_k^{lin}a_{k/2}^+\right]}{1 + \hat{a}k\left(-\frac{3}{8}kA^+\left[2v_{k/2}^{lin}v_k^{lin}t + v_{k/2}^{lin}a_k^+ + \left(1+\sqrt{2}\right)v_k^{lin}a_{k/2}^+\right]\right)t}, \tag{A 3}$$

$$v_{2k}(t) = \frac{-kA^+\left(v_k^{lin}v_k^{lin}t + 2v_k^{lin}a_k^+\right)}{1 + \hat{a}k\left(-kA^+\left(v_k^{lin}v_k^{lin}t + 2v_k^{lin}a_k^+\right)\right)t}, \tag{A 4}$$

where $\hat{a}$ is defined in (3.6).

REFERENCES

ALON, U., HECHT, J., OFER, D. & SHVARTS, D. 1995 Power laws and similarity of Rayleigh–Taylor and Richtmyer–Meshkov mixing fronts. *Phys. Rev. Lett.* **74**, 534–537.

BAI, X., DENG, X. L. & JIANG, L. 2018 A comparative study of the single-mode Richtmyer–Meshkov instability. *Shock Waves* **28**, 795–813.

BALAKUMAR, B. J., ORLICZ, G. C., RISTORCELLI, J. R., BALASUBRAMANIAN, S., PRESTRIDGE, K. P. & TOMKINS, C. D. 2012 Turbulent mixing in a Richtmyer–Meshkov fluid layer after reshock: velocity and density statistics. *J. Fluid Mech.* **696**, 67–93.

CHAPMAN, P. R. & JACOBS, J. W. 2006 Experiments on the three-dimensional incompressible Richtmyer–Meshkov instability. *Phys. Fluids* **18**, 074101.

DI STEFANO, C. A., MALAMUD, G., KURANZ, C. C., KLEIN, S. R., STOECKL, C. & DRAKE, R. P. 2015 Richtmyer–Meshkov evolution under steady shock conditions in the high-energy-density regime. *Appl. Phys. Lett.* **106**, 114103.

DIMONTE, G., FRERKING, C. E. & SCHNEIDER, M. 1995 Richtmyer–Meshkov instability in the turbulent regime. *Phys. Rev. Lett.* **74** (24), 4855–4858.

DIMOTAKIS, P. E. 2000 The mixing transition in turbulent flows. *J. Fluid Mech.* **409**, 69–98.

DING, J. C., SI, T., CHEN, M. J., ZHAI, Z. G., LU, X. Y. & LUO, X. S. 2017 On the interaction of a planar shock with a three-dimensional light gas cylinder. *J. Fluid Mech.* **828**, 289–317.

GONCHAROV, V. N. 2002 Analytical model of nonlinear, single-mode, classical Rayleigh–Taylor instability at arbitrary Atwood numbers. *Phys. Rev. Lett.* **88**, 134502.

GROOM, M. & THORNBER, B. 2020 The influence of initial perturbation power spectra on the growth of a turbulent mixing layer induced by Richtmyer–Meshkov instability. *Physica* D **407**, 132463.

HAAN, S. W. 1991 Weakly nonlinear hydrodynamic instabilities in inertial fusion. *Phys. Fluids* B **3**, 2349–2355.

HECHT, J., ALON, U. & SHVARTS, D. 1994 Potential flow models of Rayleigh–Taylor and Richtmyer–Meshkov bubble fronts. *Phys. Fluids* **6**, 4019–4030.

JACOBS, J. W. & KRIVETS, V. V. 2005 Experiments on the late-time development of single-mode Richtmyer–Meshkov instability. *Phys. Fluids* **17**, 034105.

LEINOV, E., MALAMUD, G., ELBAZ, Y., LEVIN, L. A., BEN-DOR, G., SHVARTS, D. & SADOT, O. 2009 Experimental and numerical investigation of the Richtmyer–Meshkov instability under re-shock conditions. *J. Fluid Mech.* **626**, 449–475.

LIANG, Y., ZHAI, Z., DING, J. & LUO, X. 2019 Richtmyer–Meshkov instability on a quasi-single-mode interface. *J. Fluid Mech.* **872**, 729–751.

LINDL, J., LANDEN, O., EDWARDS, J., MOSES, E. & TEAM, N. 2014 Review of the national ignition campaign 2009–2012. *Phys. Plasmas* **21**, 020501.

LIU, L., LIANG, Y., DING, J., LIU, N. & LUO, X. 2018 An elaborate experiment on the single-mode Richtmyer–Meshkov instability. *J. Fluid Mech.* **853**, R2.

LOMBARDINI, M. & PULLIN, D. I. 2009 Startup process in the Richtmyer–Meshkov instability. *Phys. Fluids* **21** (4), 044104.

LUO, X., LIANG, Y., SI, T. & ZHAI, Z. 2019 Effects of non-periodic portions of interface on Richtmyer–Meshkov instability. *J. Fluid Mech.* **861**, 309–327.

LUO, X., WANG, X. & SI, T. 2013 The Richtmyer–Meshkov instability of a three-dimensional air/SF$_6$ interface with a minimum-surface feature. *J. Fluid Mech.* **722**, R2.

MARIANI, C., VANDENBOOMGAERDE, M., JOURDAN, G., SOUFFLAND, D. & HOUAS, L. 2008 Investigation of the Richtmyer–Meshkov instability with stereolithographed interfaces. *Phys. Rev. Lett.* **100**, 254503.

MARTINEZ, D. A., SMALYUK, V. A., KANE, J. O., CASNER, A., LIBERATORE, S. & MASSE, L. P. 2015 Evidence for a bubble-competition regime in indirectly driven ablative Rayleigh–Taylor instability experiments on the NIF. *Phys. Rev. Lett.* **114**, 215004.

MCFARLAND, J. A., REILLY, D., BLACK, W., GREENOUGH, J. A. & RANJAN, D. 2015 Modal interactions between a large-wavelength inclined interface and small-wavelength multimode perturbations in a Richtmyer–Meshkov instability. *Phys. Rev.* E **92** (1), 013023.

MESHKOV, E. E. 1969 Instability of the interface of two gases accelerated by a shock wave. *Fluid Dyn.* **4**, 101–104.

MEYER, K. A. & BLEWETT, P. J. 1972 Numerical investigation of the stability of a shock-accelerated interface between two fluids. *Phys. Fluids* **15**, 753–759.

MILES, A. R., EDWARDS, M. J., BLUE, B., HANSEN, J. F., ROBEY, H. F., DRAKE, R. P., KURANZ, C. & LEIBRANDT, D. R. 2004 The effect of a short-wavelength mode on the evolution of a long-wavelength perturbatoin driven by a strong blast wave. *Phys. Plasmas* **11**, 5507–5519.

MOHAGHAR, M., CARTER, J., MUSCI, B., REILLY, D., MCFARLAND, J. & RANJAN, D. 2017 Evaluation of turbulent mixing transition in a shock-driven variable-density flow. *J. Fluid Mech.* **831**, 779–825.

NIEDERHAUS, C. E. & JACOBS, J. W. 2003 Experimental study of the Richtmyer–Meshkov instability of incompressible fluids. *J. Fluid Mech.* **485**, 243–277.

OFER, D., ALON, U., SHVARTS, D., MCCRORY, R. L. & VERDON, C. P. 1996 Modal model for the nonlinear multimode Rayleigh–Taylor instability. *Phys. Plasmas* **3** (8), 3073–3090.

PANDIAN, A., STELLINGWERF, R. F. & ABARZHI, S. I. 2017 Effect of a relative phase of waves constituting the initial perturbation and the wave interference on the dynamics of strong-shock-driven Richtmyer–Meshkov flows. *Phys. Rev. Fluids* **2** (7), 073903.

REESE, D. T., AMES, A. M., NOBLE, C. D., OAKLEY, J. G., ROTHAMER, D. A. & BONAZZA, R. 2018 Simultaneous direct measurements of concentration and velocity in the Richtmyer–Meshkov instability. *J. Fluid Mech.* **849**, 541–575.

RICHTMYER, R. D. 1960 Taylor instability in shock acceleration of compressible fluids. *Commun. Pure Appl. Maths* **13**, 297–319.

RIKANATI, A., ALON, U. & SHVARTS, D. 1998 Vortex model for the nonlinear evolution of the multimode Richtmyer–Meshkov instability at low Atwood numbers. *Phys. Rev.* E **58**, 7410–7418.

ROLLIN, B. & ANDREWS, M. J. 2013 On generating initial conditions for turbulence models: the case of Rayleigh–Taylor instability turbulent mixing. *J. Turbul.* **14**, 77–106.

SADOT, O. 2017 Experimental studies of shock wave-related phenomena at the Ben-Gurion university: a review. In *31st International Symposium on Shock Waves* (ed. A. Sasoh, T. Aoki & M. Katayama), pp. 31–44. Springer.

SADOT, O., EREZ, L., ALON, U., ORON, D., LEVIN, L. A., EREZ, G., BEN-DOR, G. & SHVARTS, D. 1998 Study of nonlinear evolution of single-mode and two-bubble interaction under Richtmyer–Meshkov instability. *Phys. Rev. Lett.* **80**, 1654–1657.

SOHN, S. I. 2003 Simple potential-flow model of Rayleigh–Taylor and Richtmyer–Meshkov instabilities for all density ratios. *Phys. Rev.* E **67**, 026301.

SOHN, S. I. 2008 Quantitative modeling of bubble competition in Richtmyer–Meshkov instability. *Phys. Rev.* E **78** (1), 017302.

THORNBER, B., DRIKAKIS, D., YOUNGS, D. L. & WILLIAMS, R. J. R. 2010 The influence of initial condition on turbulent mixing due to Richtmyer–Meshkov instability. *J. Fluid Mech.* **654**, 99–139.

THORNBER, B., GRIFFOND, J., POUJADE, O., ATTAL, N., VARSHOCHI, H., BIGDELOU, P., RAMAPRABHU, P., OLSON, B., GREENOUGH, J., ZHOU, Y., *et al.* 2017 Late-time growth rate,

mixing, and anisotropy in the multimode narrowband Richtmyer–Meshkov instability: the θ-group collaboration. *Phys. Fluids* **29** (10), 105107.

VANDENBOOMGAERDE, M., GAUTHIER, S. & MÜGLER, C. 2002 Nonlinear regime of a multimode Richtmyer–Meshkov instability: a simplified perturbation theory. *Phys. Fluids* **14** (3), 1111–1122.

WOUCHUK, J. G. 2001 Growth rate of the linear Richtmyer–Meshkov instability when a shock is reflected. *Phys. Rev. E* **63**, 056303.

YANG, J., KUBOTA, T. & ZUKOSKI, E. E. 1993 Application of shock-induced mixing to supersonic combustion. *AIAA J.* **31**, 854–862.

ZHANG, Q., DENG, S. & GUO, W. 2018 Quantitative theory for the growth rate and amplitude of the compressible Richtmyer–Meshkov instability at all density ratios. *Phys. Rev. Lett.* **121** (17), 174502.

ZHANG, Q. & GUO, W. 2016 Universality of finger growth in two-dimensional Rayleigh–Taylor and Richtmyer–Meshkov instabilities with all density ratios. *J. Fluid Mech.* **786**, 47–61.

ZHOU, Y., CLARK, T. T., CLARK, D. S., GLENDINNING, S. G., SKINNER, M. A., HUNTINGTON, C. M., HURRICANE, O. A., DIMITS, A. M. & REMINGTON, B. A. 2019 Turbulent mixing and transition criteria of flows induced by hydrodynamic instabilities. *Phys. Plasmas* **26**, 080901.

ZHOU, Y., REMINGTON, B. A., ROBEY, H. F., COOK, A. W., GLENDINNING, S. G., DIMITS, A., BUCKINGHAM, A. C., ZIMMERMAN, G. B., BURKE, E. W., PEYSER, T. A., *et al.* 2003 Progress in understanding turbulent mixing induced by Rayleigh–Taylor and Richtmyer–Meshkov instabilities. *Phys. Plasmas* **10**, 1883–1896.